INL/JOU-25-82808-Revision-1

# 3D Pore Structure in EBR-II U-19Pu-10Zr Fuel Fluff Region by X-ray Micro-Computed Tomography

January 2026

Jake Thornton Fay, Cameron Boyd Howard, Colby B Jensen, Luca Capriotti, Jie Lian, William C Chuirazzi

Changing the World's Energy Future

Idaho National Laboratory

*INL is a U.S. Department of Energy National Laboratory operated by Battelle Energy Alliance, LLC*

INL/JOU-25-82808-Revision-1

# 3D Pore Structure in EBR-II U-19Pu-10Zr Fuel Fluff Region by X-ray Micro-Computed Tomography

**Jake Thornton Fay, Cameron Boyd Howard, Colby B Jensen, Luca Capriotti, Jie Lian, William C Chuirazzi**

**January 2026**

**Idaho National Laboratory**
**Idaho Falls, Idaho 83415**

**http://www.inl.gov**

**Prepared for the**
**U.S. Department of Energy**
**Under DOE Idaho Operations Office**
**Contract DE-AC07-05ID14517**

# 3D Pore Structure in EBR-II U-19Pu-10Zr Fuel Fluff Region by X-ray Micro-Computed Tomography

Jake Fay[1 2], William Chuirazzi[2], Luca Capriotti[2], Fidelma Di Lemma[2], Cameron Howard[2], Mario Matos[2], Jie Lian[1]

[1] Department of Mechanical, Aerospace & Nuclear Engineering, Rensselaer Polytechnic Institute, Troy, NY 12180

[2] Idaho National Laboratory, Idaho Falls, ID 83415, USA

## Abstract

Metallic fuels comprised of U-Zr binary and U-Pu-Zr ternary alloys are a promising fuel candidate for sodium cooled fast reactors and possess many advantages over ceramic fuels such as higher uranium density and improved thermal conductivity. Fluff is a highly porous structure that forms at the top of metallic fuel slugs during irradiation and has been seen extensively in past SFR experiments such as EBR-II. Previous investigations have shown that fluff is comprised of fuel fragments and is correlated with fuel burnup and Pu content, but the exact formation mechanisms behind fluff formation are still poorly understood. In this work cube shaped lift outs were taken from the fluff and bulk fuel regions of a high burnup U-19Pu-10Zr EBR-II fuel slug and examined by X-ray microcomputed tomography and surface SEM and EDS. Surface EDS showed minimal differences between the elemental compositions of the fluff and fuel cubes. Three-dimensional (3D) pore analysis from the tomography scans however showed significant differences between the fluff and fuel cube pore size distributions even at the microscale. The high porosity and irregular pore distribution seen in macroscale fluff was also present within the micro-scale fluff cube with it having a much higher porosity than the fuel cube which was concentrated in a few large pore networks.

## 1. Introduction

### 1.1 Metallic Fuels Behavior and Fluff

U-Zr and U-Pu-Zr metallic fuels have been key components of many Sodium Fast Reactor (SFR) experiments and hold numerous advantages over ceramic fuels such as $UO_2$ in liquid metal cooled reactor systems. Their thermal conductivities are an order of magnitude higher allowing for lower peak fuel temperatures and gradients during operation [1]. They are chemically compatible with liquid sodium, improving safety performance following cladding failure [1]. They produce a harder neutron spectrum which improves breeding ratios for fissile isotopes [2]. Finally, they have a higher uranium density allowing for lower enrichment or more

compact cores. For these reasons the Experimental Breeder Reactor II experiment (EBR-II) and other past SFR research reactors extensively explored the use of metallic fuels during their operation [3]. Nuclear energy startups such as TerraPower and Oklo also propose using metallic fuels in their advanced reactor designs.

Metallic fuels exhibit significantly different swelling behaviors compared to ceramic fuels. During early burnup metallic fuels swell rapidly from the formation of pores from fission gas. As irradiation continues the pores grow and coalesce with neighboring pores to form large, interconnected pore networks [4]. Between 1 and 2 % at. burnup the pore networks become fully interconnected, and the trapped fission gas is vented from the fuel, drastically slowing the swelling rate. Intense fuel swelling proved a challenge for the first metallic fueled reactors. In EBR-I rapid early swelling exerted intense pressure on the cladding leading to early fuel pin failure [1]. Subsequent metallic fuel experiments resolved this issue by reducing the diameter of the fuel slugs to allow room for early fuel expansion. Fuel smeared density, defined as the ratio of the fresh fuel slug cross sectional area to the cross-sectional area available in the cladding tube, characterizes this reduction in fuel diameter [5]. Fuel pins were also designed with large plenums to accommodate the large fission gas buildup [5] [2]. Finally liquid sodium was bonded to the fuel slug to maintain acceptable thermal contact between fuel and cladding at beginning of life [1].

During the operation of EBR-II an irregular structure was seen to form at the top of most metallic fuel pins, extending from between a few millimeters to several centimeters above the top of the fuel slug. This structure, designated as fluff, is a highly porous foam that grows on the top of metallic fuel pins during irradiation. Di Lemma et al [6] performed Scanning Electron Microscopy (SEM) and Electron Probe Micro-Analysis (EPMA) characterizations of this structure showing that fluff is predominantly composed of fuel components in addition to migrated Fission Products (FP). Further work by [7] and [8] characterized the fluff content on a collection of EBR-II pins using radiograph images to determine correlations between pin operating conditions and the extent of fluff formation. From this work it was found that fluff content increases gradually with increasing burnup and that fluff formation is higher in U-Zr binary fuels compared to U-Pu-Zr ternary fuels. It was also found that pins that had been operated at abnormally high temperature (EBR-II subassembly X447) exhibited little to no fluff indicating a possible negative high temperature correlation [7]. While these correlations have provided solid insight, additional Post Irradiation Examination (PIE) of fluff samples needs to be collected to determine its precise formation mechanisms. Besides EBR-II fluff, similar fluff has also been seen extensively in other metallic fuel irradiation experiments such as the Fast Flux Test Facility (FFTF) [9], suggesting that this phenomenon is a more global effect warranting further investigations.

Since fluff is predominantly composed of fuel components it could influence reactivity in future SFR designs. Fluff's high porosity and inherent structural fragility could also cause it to detach from the fuel column and eject into the plenum during temperature transients and accident scenarios. To address these issues more information needs to be determined about the properties of fluff and its formation mechanisms. To date, limited Post Irradiation Examination (PIE) has

been collected from the fluff structure consisting of SEM and EPMA on a single sample and non-destructive neutron radiographs. This project involved the first ever 3D reconstruction of fluff by X-ray Micro-Computed Tomography (Micro-CT) which was accompanied by localized SEM and Energy Dispersive Spectroscopy (EDS) of the Micro-CT samples.

While fluff has been widely seen in metallic fuel PIE its formation mechanisms are still not well understood. Work correlating fluff quantity with reactor operating conditions using EBR-II legacy data in [7] postulated 2 possible fluff formation theories. The first theory is that when the fuel expands to encounter the cladding the frictional forces between the fuel and cladding cause a localized region of high stress at the top of the fuel slug. This region of high stress undergoes fuel creep at a faster rate than the rest of the fuel slug causing it to fragment and form the highly porous fluff region. As the fuel continues to swell axially this region of high stress expands to impact more fuel and progressively expands the fluff region. The work in [7] supported this formation theory with the findings that fluff increases continuously with burnup, and that there is more fluff observed in U-Zr alloys which are known to undergo greater axial swelling compared to U-Pu-Zr fuels [10]. Computational research in [7] also performed simulations with the fuel code BISON [11] that showed stress concentrations at the top of the fuel pin when high frictional forces are imposed between fuel and cladding.

A second theory of fluff formation is that local pressure from fission gases at the top of the fuel slug causes the top to burst sending small fuel fragments into the plenum. After the local fission gas pressure is released the top of the fuel fuses due to the high plasticity of metallic fuels [12]. This leads to new pressure build up and the process repeats slowly increasing the quantity of loose fuel fragments at the top of the fuel. Metal foams can be much more buoyant than their solid counter parts. Aluminum foams have been fabricated that are capable of floating in water [13]. The highly porous fine fuel fragments could undergo a similar phenomenon where they gain increased mobility in the sodium bond, grouping together to form the fluff structure. The fragments' mobility could be further assisted by the continuous venting of newly created fission gas. This theory is similarly supported by the finding that fluff increases progressively with burnup. Recently [8] expanded on the work done [7] by creating an automatic image analysis algorithm that could measure fluff content directly from radiographs with reduced uncertainty and applied this algorithm to a larger quantity of EBR-II radiographs. Additional findings indicated that there is a positive relationship between axial swelling and fluff content which supports the creep driven formation mechanism.

### 1.2 X-ray Micro-Computed Tomography Theory

X-ray Micro-Computed Tomography (Micro-CT) is a non-destructive characterization tool that can be used to determine the 3D geometry and relative phase composition of a sample using the X-ray attenuation contrasts between its material phases. Micro-CT has seen extensive use in the medical industry and more recently has been used in nuclear materials and fuels characterization [14]. It works by sending a collimated X-ray beam into the sample and detecting the transmitted X-rays. The sample is then rotated through 360$^{o}$ while 2D radiographs are collected at finite degree increments. The radiographs are then mathematically reconstructed to produce a 3D image of the sample microstructure based on the X-ray attenuation difference of

the sample's constituent phases. The overall magnification of the radiographs can be controlled by varying the distance between the sample and detector, since this system uses geometric magnification. The further the sample is from the detector the higher the magnification [15] [16].

X-ray attenuation is primarily driven by electron interactions increasing with sample Z value and physical density [15] [17], according to the Beer-Lambert law [18]. In the past it has been difficult to characterize metallic fuel samples with laboratory based Micro-CT systems because the high X-ray attenuations of uranium and plutonium prevent enough X-rays from reaching the detector to form a reliable image. Past metallic fuel Micro-CT characterizations have relied on the higher photon flux synchrotron X-ray sources [19]. Synchrotron beamlines have successfully performed tomography on U-10Zr and U-Mo samples [19] [20]. The fluff cubes characterized in this study had high porosities and small sizes ($60\times60\times60\mu m$ cubes) which allowed for the successful characterization with laboratory Micro-CT as the smaller samples enabled X-rays to transmit through the sample and reach the detector. Previous work [20] has shown the effectiveness of using synchrotron generated X-rays in characterizing pores and finding relative concentrations of U and Zr in irradiated metallic fuels. While the laboratory Micro-CT used in this characterization could not differentiate between specific fuel phases it was effective in distinguishing between pores and solid fuel.

# 2. Methods

## 2. Sample History

The sample used in this study was a longitudinal cross section cut from the top of EBR-II parent pin X512-DP55 shown in Figure 1. X512-DP55 was originally fabricated as an EBR-II fuel pin that was irradiated in sub-assembly X441 [6] [21]. Its design parameters consisted of U-19Pu-10Zr fuel composition (19 wt.% Pu 10 wt.% Zr), 75% smear density, and HT9 cladding. DP55 reached an approximate peak burnup of 11.1 at. % during its irradiation in X441. In 1992 this fuel rod was used as part of the X512 transient overpower test in EBR-II termed the Overpower Transient Test (OPT-1) [21]. OPT-1 consisted of a slow over-power transient meant to mimic a malfunctioning control rod drive. Fuel was preconditioned at normal operating power for 24 hours, then it was subjected to a slow over-power event that lasted 24 hours and peaked at 32% overpower. Table 1 gives the heating and temperature details of the transient test [6] [21]. DP55 was radiographed before and after the transient experiments. Fluff was seen on DP55 prior to the transient and the post transient radiograph showed minimal changes in the fluff structure [6] indicating that fluff did not form during the transient test.

*Table 1: X512-DP55 Pin Conditions During OTT [21]*

| | Fuel/cladding composition | LHR (kW/m) | Fuel Centerline Temp (ºC) | Clad I.D. Temp (ºC) | Clad O.D. Temp (ºC) | Coolant Temp (ºC) |
|---|---|---|---|---|---|---|
| Pre-Conditioning (54 MWt) | U19Pu10Zr/HT9 | 41.7 | 746 | 567 | 548 | 539 |

| | | | | | | |
|---|---|---|---|---|---|---|
| Transient Peak (71 MWt) | U19Pu10Zr/HT9 | 54.8 | 862 | 629 | 606 | 596 |

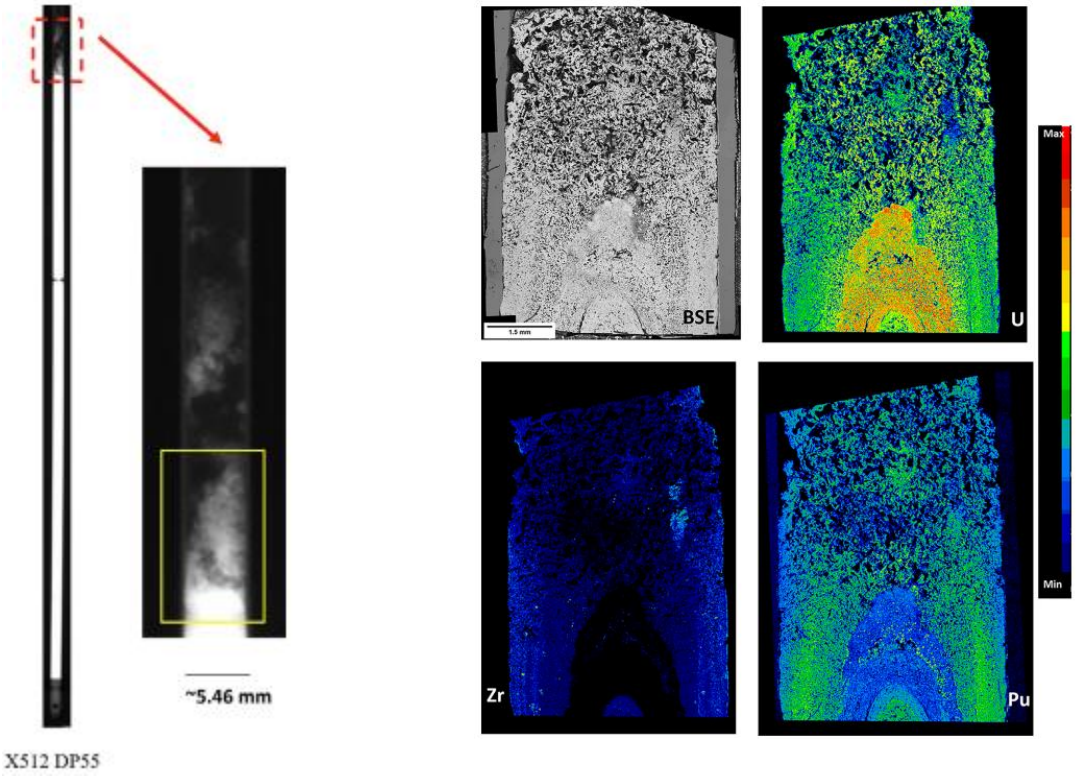


*Figure 1: Radiograph of pin X512 DP55 and location of longitudinal region sectioned to make MNT38A (recreated from [6])*

In 2020 DP55 underwent a series of PIE focused on the top of the fuel slug. A cross section containing fluff was sectioned from the top of DP55 and imaged by optical microscopy in the Hot Fuels Examination Facility (HFEF) at INL. Following this the fluff sample was transferred to the Irradiated Materials Characterization Laboratory (IMCL) where it was characterized by SEM and EPMA. Qualitative elemental maps were collected from the entire fluff cross section, which are recreated in Figure 1, and quantitative elemental data was collected from key points. The details of this work are discussed in [6], which determined that the fluff region is primarily comprised of fuel elements (U, Pu, and Zr). No clear signs of fuel melting were identified in this work.

## 2.3 Sample Characterization and Preparation

All sample preparations and characterizations for this project were performed in IMCL. First the fluff cross section from Figure 1 was taken from storage and polished with ethanol lubricant in the shielded sample preparation area at IMCL. This removed surface oxidation formed between the end of the characterization work done in [6] and the start of this project. Following polishing, the sample was transferred to the shielded ThermoFisher G3 Plasma Focused Ion Beam (PFIB). A Xe ion beam was used to trench and lift out two 60×60×60µm cubes for further characterization. This step was needed to produce lower activity sub-samples and to create samples thin enough to enable Micro-CT characterization. Figure 3 shows an SEM

montage of the entire fluff cross section and of the relative locations of the two cube lift-outs. The first cube was taken from high in the fluff section and is referred to as the “fluff cube” for the remainder of this paper. The second cube was taken near the base of the mount near the fuel periphery. Since this cube was taken from bulk fuel it is referred to as the “fuel cube” for the remainder of this paper. Following lift out, each cube was mounted on a separate Mo Transmission Electron Microscopy (TEM) grid. The cubes were each mounted at the highest vertical point of the respective grids to support characterization by Micro-CT. During the mounting process a portion of the fluff cube was accidentally milled out by the ion beam due to beam drift. This damaged region was left in place during subsequent Micro-CT collection, but the data pertaining to the damaged region was cropped out during post processing. Appendix A shows the damaged region and its removal from the CT reconstructions.

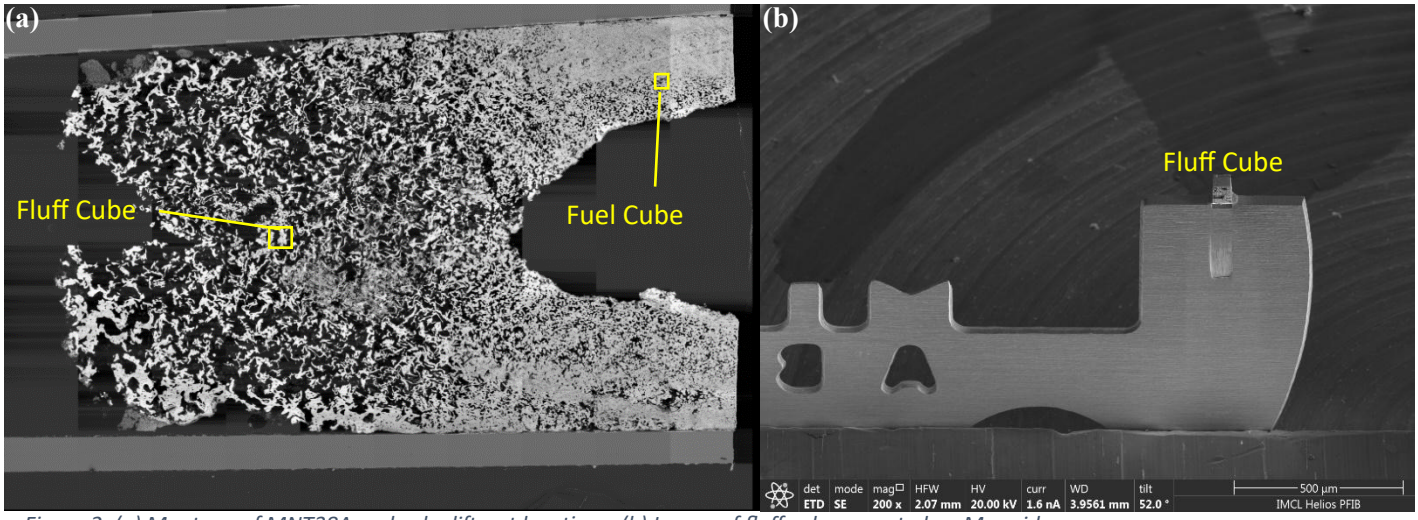


*Figure 2: (a) Montage of MNT38A and cube lift-out locations. (b) Image of fluff cube mounted on Mo grid.*

## 2.3 Micro-Computed Tomography

The two cubes were characterized by Micro-CT using the ZEISS Xradia 620 Versa X-ray Microscope (XCT) installed on the floor of IMCL. The XCT is designated as a non-rad instrument so both cubes had to be encased in a plastic capsule to prevent the spread of contamination in the XCT chamber. The XCT is equipped to operate with a flat panel detector that can do large field of view scans at resolutions down to 6 µm/voxel, or an X-ray microscope that can do small field of view scans at resolutions down to 260 nm/voxel [22]. Since the 2 cubes are micron-sized, all CT scans used the X-ray microscope to maximize resolution. The XCT produces a poly-energetic X-ray beam in a Bremsstrahlung X-ray spectrum with a maximum X-ray energy of 160keV. Because of the Bremsstrahlung spectrum, the voxel gray-scale values from the XCT reconstruction could not be easily attributed to a specific X-ray attenuation value, which is common in Micro-CT reconstructions made using mono-energetic synchrotron sources [20] [19] [22].

Both cubes were subjected to identical scans which consisted of an initial fast low-resolution scan (530 nm/voxel), then a slower high-resolution scan (260 nm/voxel). Both scans produced similar results, so only the high-resolution scan was used in data analysis since it resolved finer features. For the high resolution scans the cubes were rotated 360 degrees while a

total of 3201 X-ray attenuation images were collected. Following this, the vendor supplied ZEISS Scout and Scan Control System Reconstructor Software was used to reconstruct the collection of 2D radiographs into a 3D image with a final resolution of 265 nm/voxel. The reconstruction software uses a proprietary algorithm that involves applying data smoothing and beam artifact corrections [23], and then converting the data to a 3D image using a modified Feldkamp-Davis-Kress (FDK) algorithm [24]. The 3D reconstructions of both lift-outs were saved as of stacks of 2D .tiff images in the Z direction. The fluff cube stack consisted of 290 separate 16-bit 221×230 pixel images and the fuel cube stack consisted of 322 separate 16 bit 252×270 pixel images. Due to the small size of the cubes, high attenuation of uranium and plutonium, and resolution limits of laboratory Micro-CT, only pores and solid fuel could be distinguished in the recreated 3D image. Individual phases within the fuel could not be resolved.

### 2.4 Micro-CT Image Analysis:

All image analysis in this project was performed using the open-source image analysis software Fiji [25] and the image analysis toolbox application in MATLAB [26]. Following Micro-CT scans, the 3D reconstructions of the fluff and fuel cubes were output in the form of 2D .tiff image stacks in the Z direction. The first step in image processing involved using MATLAB to apply a Weiner noise reduction filter [27] to each image in both stacks to reduce noise and enhance the contrast between solid fuel and pores. Following this, several binarization algorithms utilizing both global thresholding and adaptive thresholding algorithms were used to segment pores from solid fuel in the image stacks. Segmentations were all evaluated via visual inspection. In addition 5 frames from each image stack were manually segmented by hand and used to quantitatively evaluate the quality of each segmentation algorithm. The MATLAB adaptive thresholding algorithm “adaptthresh” produced the most successful pore segmentations on both cubes [26] [28]. Appendix B shows the evaluation of the adaptthresh segmentation compared to the manually segmented images. Following pore segmentation, connected structure algorithms in Fiji and MATLAB were used to identify each pore structure as well as calculate key properties such as pore volume and pore surface area. These algorithms consisted of the “3D Object Counter” in Fiji [25], the “bwconncomp” and “regionprops3” commands in MATLAB [26], and the BoneJ plugin from Fiji [29]. All 3 algorithms produced identical results for pore volumes and surface areas. All 3D porosity figures in this paper were created with the MATLAB image analysis toolbox.

### 2.5 EDS

Following Micro-CT scans both cubes were transferred to a ThermoFisher G4 Helios Hydra PFIB. First the ion beam was used to polish and smooth the front surface of both cubes. Then the cubes were positioned so that their front faces were perpendicular to the electron beam and the accelerating voltage was set to 20 keV. EDS maps of fuel elements (U, Pu, Zr) and major fission products were collected on the entirety of the cube faces. Following this, 30 EDS point spectra were taken on each of the 2 cube front faces, focusing on areas of unique phase composition and FP enrichment. Each point spectra had a live time of 50 sec.

# 3 Results

## 3.1 EDS Characterization

Figure 4 and Figure 5 show qualitative EDS scans collected from the faces of the fluff and fuel cubes. The fuel cube is primarily made up of fuel elements U, Pu, and Zr with an overall Zr content slightly higher than the as-cast concentration. This is expected since this lift-out was taken from the outer periphery region of the fuel which tends to become rich in Zr due to constituent redistribution during reactor operation [30]. EDS maps also revealed FP rich precipitates. The most common fission products were lanthanides, particularly Nd, that tended to collect in precipitates near pores. This is represented by the Nd map in Figure 4. Significant quantities of La, Ce and to a lesser extent Pr and Sm were also seen, but their distributions in the fuel cube line up identically with the Nd distribution so their maps are not shown. The grouping of lanthanides in precipitates near pore structures has been seen extensively in past bulk fuel PIE [30] [31] [32]. This concentration near pores is in line with the current understanding of lanthanide transport where lanthanides undergo liquid like transportation through interconnected pore structures and group together in lanthanide precipitates [33]. The fuel cube also showed a high Te and Ba concentration in select areas.

Semi-quantitative point spectra were also collected, and a representative subset is summarized in

. Most spectra in the fuel cube showed concentrations of U, Pu, and Zr in proportions

| | Fluff Cube | | | | | | Fuel Cube | | | | | |
|---|---|---|---|---|---|---|---|---|---|---|---|---|
| Element | 1 | 2 | 3 | 4 | 5 | 6 | 1 | 2 | 3 | 4 | 5 | 6 |
| U | 18.5 | 68 | 52.7 | 28.5 | 70.9 | 69 | 22.3 | 61.6 | 62.4 | 62.9 | 19.2 | 39.7 |
| Pu | 7.9 | 22.7 | 18.2 | 11.6 | 22.6 | 23.4 | 13.4 | 19.1 | 25.9 | 26.6 | 7.8 | 22.7 |
| Zr | 1.5 | 9.3 | 27.2 | 3.9 | 6.5 | 7.6 | 9.8 | 17.7 | 11.7 | 10.5 | 13.1 | 33.2 |
| Lanthanide | 69.9 | 0 | 0.8 | 37.9 | 0 | 0 | 2.8 | 1.2 | 0 | 0 | 58.9 | 3.5 |
| Ba | 2.2 | 0 | 1.1 | 0 | 0 | 0 | 26.3 | 0 | 0 | 0 | 1 | 0.9 |
| Pd | 0 | 0 | 0 | 18.1 | 0 | 0 | 0 | 0.4 | 0 | 0 | 0 | 0 |
| Te | 0 | 0 | 0 | 0 | 0 | 0 | 25.4 | 0 | 0 | 0 | 0 | 0 |

similar to as cast fuel with small quantities of fission products such as spectra 3 and 4. The remaining spectra showed either regions of higher Zr enrichment and medium concentrations of FPs such as spectra 2 and 6 or were predominantly comprised of lanthanides such as spectra 5. The most outlying spectra on was 1 which had a large Te and Ba concentration and was located near a pore. A previous TEM characterization of high burnup U-10Zr fuel found small BaTe precipitates [31], so it is possible the region in spectra 1 is rich in BaTe. The in-pile transport behaviors of Te and Ba are not well characterized in metallic fuel, but both are expected to be highly soluble in sodium [34]. It is possible that dissolved Te and Ba were transported to the top of the fuel slug as sodium was displaced by fuel swelling. The elements could have then precipitated out as BaTe when the fuel cooled following shutdown.

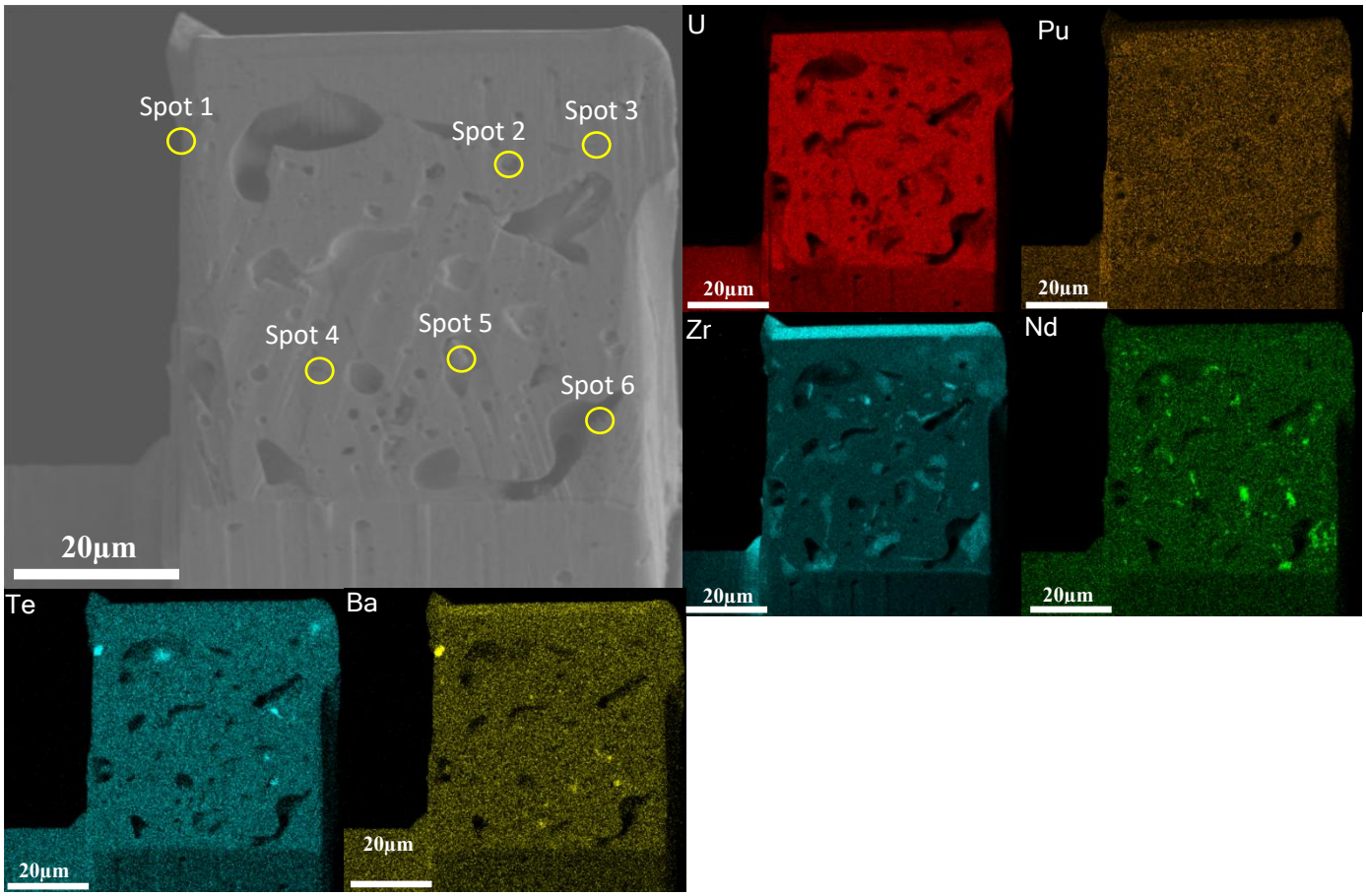


*Figure 3: Fuel Cube EDS Maps of Key Elements*

The elemental composition of the fluff cube was similar to that of the fuel cube, being predominantly made up of fuel elements with lanthanide FPs concentrated near pore structures. The Zr content of the fluff cube overall was higher than as cast fuel which was expected due to constituent redistribution from the cooler temperatures at the top of the pin [30]. A key difference between the fluff and fuel cubes was that the fluff cube did not have any areas of high Te concentration, though it did have areas of high Ba concentration. The point spectra collected from the fluff cube showed similar results to the fuel cube with most spectra showing near as-cast concentrations of fuel elements (spectra 2, 5 and 6), and the remaining spectra showing

either high Zr concentrations (spectra 3) or lanthanide concentrations (spectra 1 and 4). The lanthanide precipitates in the fluff cube also showed a large portion of Pd, particularly in spectra 4. Pd presence is expected since it is known to bind with lanthanides and is even being examined as a possible fuel additive to reduce lanthanide driven FCCI [33]. Small amounts of Pd were also seen in the fuel cube, but no areas of high Pd concentration similar to spectra 4 obtained from the fluff cube were seen.

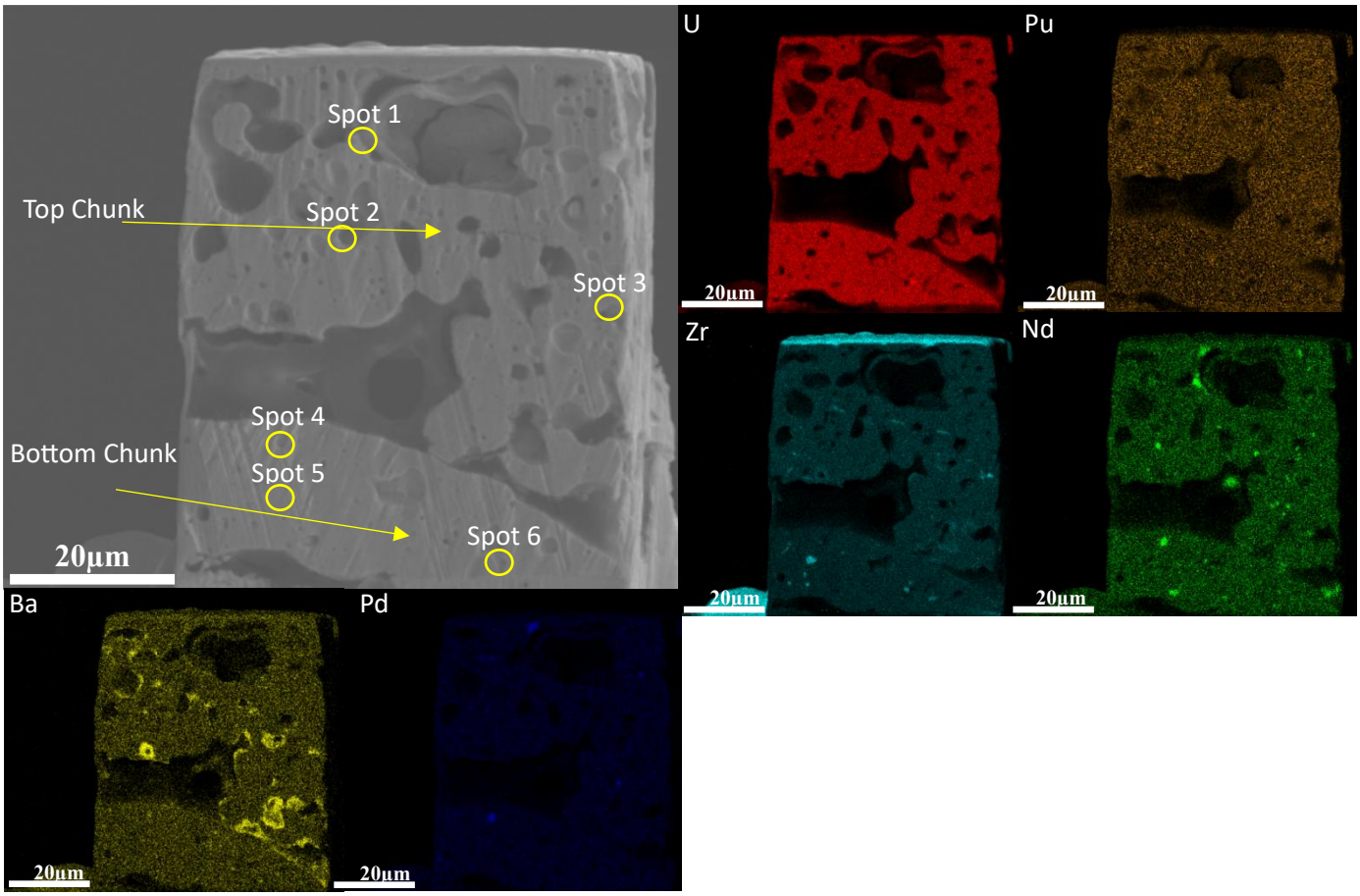


*Figure 4: Fluff Cube EDS Maps of Key Elements*

| | Fluff Cube | | | | | | Fuel Cube | | | | | |
|---|---|---|---|---|---|---|---|---|---|---|---|---|
| Element | 1 | 2 | 3 | 4 | 5 | 6 | 1 | 2 | 3 | 4 | 5 | 6 |
| U | 18.5 | 68 | 52.7 | 28.5 | 70.9 | 69 | 22.3 | 61.6 | 62.4 | 62.9 | 19.2 | 39.7 |
| Pu | 7.9 | 22.7 | 18.2 | 11.6 | 22.6 | 23.4 | 13.4 | 19.1 | 25.9 | 26.6 | 7.8 | 22.7 |
| Zr | 1.5 | 9.3 | 27.2 | 3.9 | 6.5 | 7.6 | 9.8 | 17.7 | 11.7 | 10.5 | 13.1 | 33.2 |

| | | | | | | | | | | | | |
|---|---|---|---|---|---|---|---|---|---|---|---|---|
| Lanthanide | 69.9 | 0 | 0.8 | 37.9 | 0 | 0 | 2.8 | 1.2 | 0 | 0 | 58.9 | 3.5 |
| Ba | 2.2 | 0 | 1.1 | 0 | 0 | 0 | 26.3 | 0 | 0 | 0 | 1 | 0.9 |
| Pd | 0 | 0 | 0 | 18.1 | 0 | 0 | 0 | 0.4 | 0 | 0 | 0 | 0 |
| Te | 0 | 0 | 0 | 0 | 0 | 0 | 25.4 | 0 | 0 | 0 | 0 | 0 |

*Table 2: Semi-Quantitative Point Spectra for Fluff and Fuel Cubes (wt. %)*

### 3.2 3D Representation of Both Lift-Outs

Figure 6 shows the 3D images of the fluff and fuel cubes that were generated from the Micro-CT scans. The fluff cube was found to be comprised of two distinct regions that were barely connected at 2 points as shown in Figure 6b. While the 2 regions are connected they showed significantly different pore characteristics with the bottom region have a much smaller overall porosity compared to the top region. Because of this, pore analysis was first executed by treating the fluff cube as a single unit that treated the space between regions as a continuation of porosity. Next, the fluff cube was separated into a top and bottom region as shown in Figure 6e and Figure 6f, and pore structure analysis was performed on the 2 regions separately. This made it possible to quantify the differences between the top and bottom regions.

Figure 6c and Figure 6d show the same front faces of the fuel and fluff cube that were characterized by SEM in Figure 4 and Figure 5. Overall there is good agreement in the location and appearance of the major pore structures between the SEM images and the Micro-CT reconstruction, though there are some noticeable deviations between the 2 characterizations such as the surface roughness of the Micro-CT reconstruction and the size and shape of the smaller pores. These deviations are due to 2 reasons. The first is that the front surfaces of the two cubes were smoothed by ion-beam prior to collecting the SEM, which was done after the Micro-CT scans were collected. Because of this the SEM micrographs in Figure 4 and Figure 5 show a region 1-2µm below the surfaces shown in the Micro-CT reconstructions in Figure 6c and Figure 6d. The other reason is SEM can achieve a much higher resolution compared to Micro-CT.

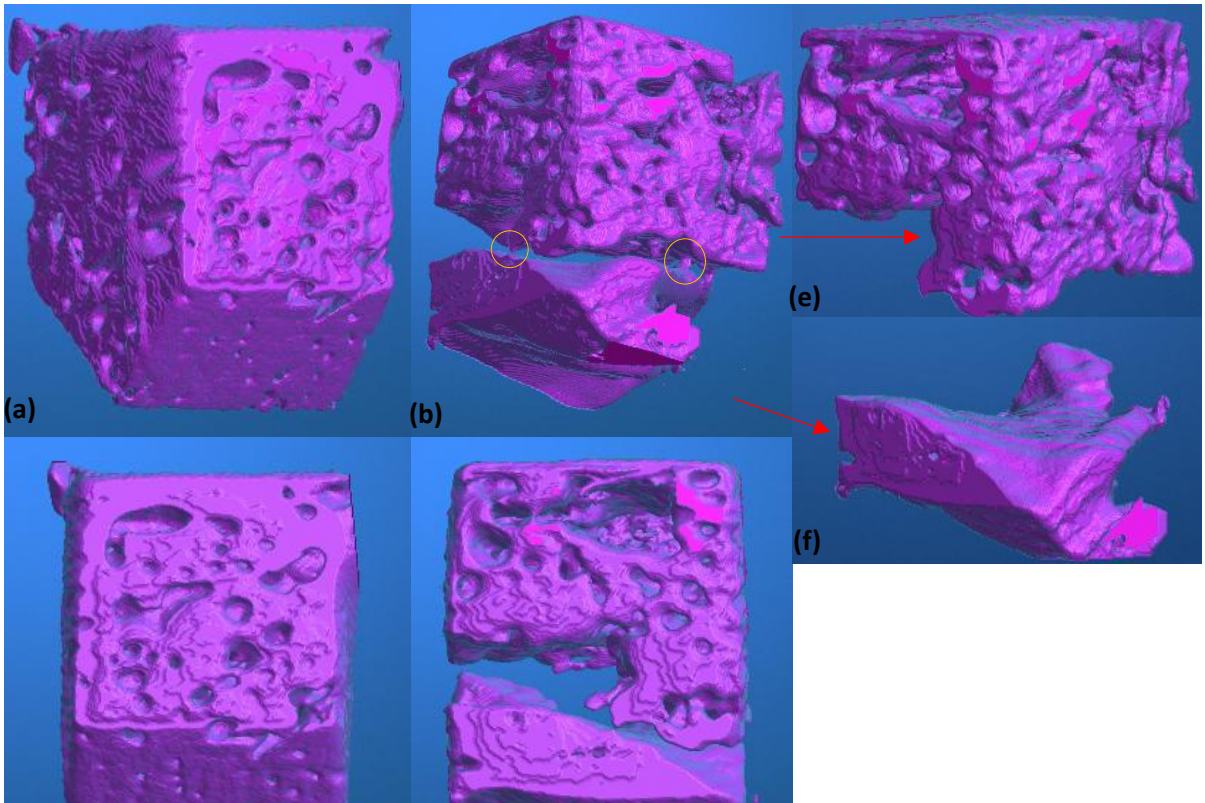

*Figure 5: 3D Reconstructions of lift-outs in front and side orientations. (a) Fuel cube rotated, (b) fluff cube rotated with points connecting the top and bottom region circled, (c) Fuel cube front face, (d) Fluff cube front face, (e) Fluff cube top region, (f) fluff cube bottom region.*

### 3.3 Pore Characterization

The pore structure analysis performed on each cube consisted of 4 steps: (1) Calculating overall porosity, (2) identifying and measuring the volume of each connected pore network, (3) distinguishing between closed pores and open pores and their relative contribution to overall porosity, and (4) calculating sphericity for each pore.

The overall porosity calculation was performed according to eq. 1 where $V_p$ is the summed volume of all porosity and $V_S$ is the summed volume of solid fuel. Pore identification and volume measurements were performed using 3 different image characterization algorithms. These consisted of the MATLAB *regionprobs3* command, the Fiji *3D objects counter*, and the particle analyzer command in the Fiji plugin *BoneJ* [26] [25] [29]. These algorithms defined pore voxels as connected if they touched another pore voxel on any side or corner and calculated pore volume based off the voxel count in each pore structure. All 3 pore identification algorithms yielded identical pore counts, pore volumes, and surface areas. Due to the resolution of the XCT and additional uncertainty from the segmentation process, only pore structures with greater than 10 voxels were counted. A closed pore structure is defined in this paper as a pore structure that does not connect with the outer surface of the cube. These structures have significance as they were still in the process of growing, and their entire volume is enclosed in their respective cube. Closed structures are also more likely to contain trapped fission gases which could be of note in future analysis. Open pore structures are defined as pore structures that do connect with the lift-out surface and hence provide fission gases with a path of escape. Their total volume with respect to the entire fuel slug is also greater than what can be measured from the 3D reconstructions.

*Equation 1*

$$Porosity = \frac{V_p}{V_p + V_S}$$

Sphericity is a measure of how closely a pore network resembles a spherical geometry. It can be calculated using eq. 2 where $V$ is the volume of the pore structure, $SA$ is the surface area of the pore, and $SA_s$ is the surface area of an ideal sphere that has an identical volume to the pore structure. Sphericity values range from 0 to 1 with 1 being a perfect sphere. Because of this, sphericity can be used to characterize the extent of pore interconnection since small closed pores

tend to be more spherical while large interconnected pore networks have irregular shapes [20] [35].

*Equation 2*

$$Sphericity = \frac{SA_s}{SA} = \frac{(36\pi V^2)^{\frac{1}{3}}}{SA}$$

### 3.4 3D Pore Representations and Key Statistics

Table 3 gives a summary of the pore analysis listed in the previous section and Figure 7 gives a 3D representation of pore structures in each cube. The first column in Figure 7 shows the largest single interconnected pore structure, the second column shows the next 4 largest pore structures, and the final column shows all remaining pore structures. The fuel cube was found to have 512 separate pore structures that combined to form an overall porosity of 15%. 69% of this overall porosity was concentrated in the largest 5 open pore structures while the remaining 31% was distributed within the other 507 open and closed pores. Closed pore structures were found to make up 23% of total porosity while open structures made up the remaining 77%. This heterogeneous pore size distribution is characteristic of what has been seen in SEM images of bulk fuel cross sections. Previous SEM characterizations of high burnup fuel cross sections show that the majority of fuel porosity is concentrated in a small number of large, interconnected pores while the majority of discrete pore structures are small isolated pores [31].

Pore network analysis on the fluff cube as a single unit showed that it contains 182 separate pore structures that add up to a total porosity of 36% which was almost completely contained in open pore networks. The fluff cube also showed higher porosity concentration compared to the fuel cube with 95% of the total porosity contained in the largest pore network that occupies the empty space inside the top fuel chunk and the space between the top and bottom fuel chunk. Closed pore structures comprised only 2% of total porosity.

Pore network analysis of the fluff cube treating the top and bottom regions as two separate units showed notable differences in the pore behavior of the two fluff regions. The top region closely resembled the pore behavior of the full fluff cube with an overall porosity of 32% that was mostly concentrated in a single large pore network. The bottom region was much denser, even compared to the fuel cube, with only 8% porosity. The porosity was also less concentrated in the largest pore networks and had a closed porosity that was larger than the total fluff cube but less than that of the fuel cube.

*Table 3: Summary of Pore Analysis Results for Fuel and Fluff Cubes*

| | Fuel Cube | Fluff Cube | Fluff Cube Bottom Region | Fluff Cube Top Region |
|---|---|---|---|---|
| Number of pores | 512 | 182 | 83 | 108 |
| Total porosity | 15% | 36% | 8% | 32% |
| % Open porosity | 77% | 98% | 87% | 97% |

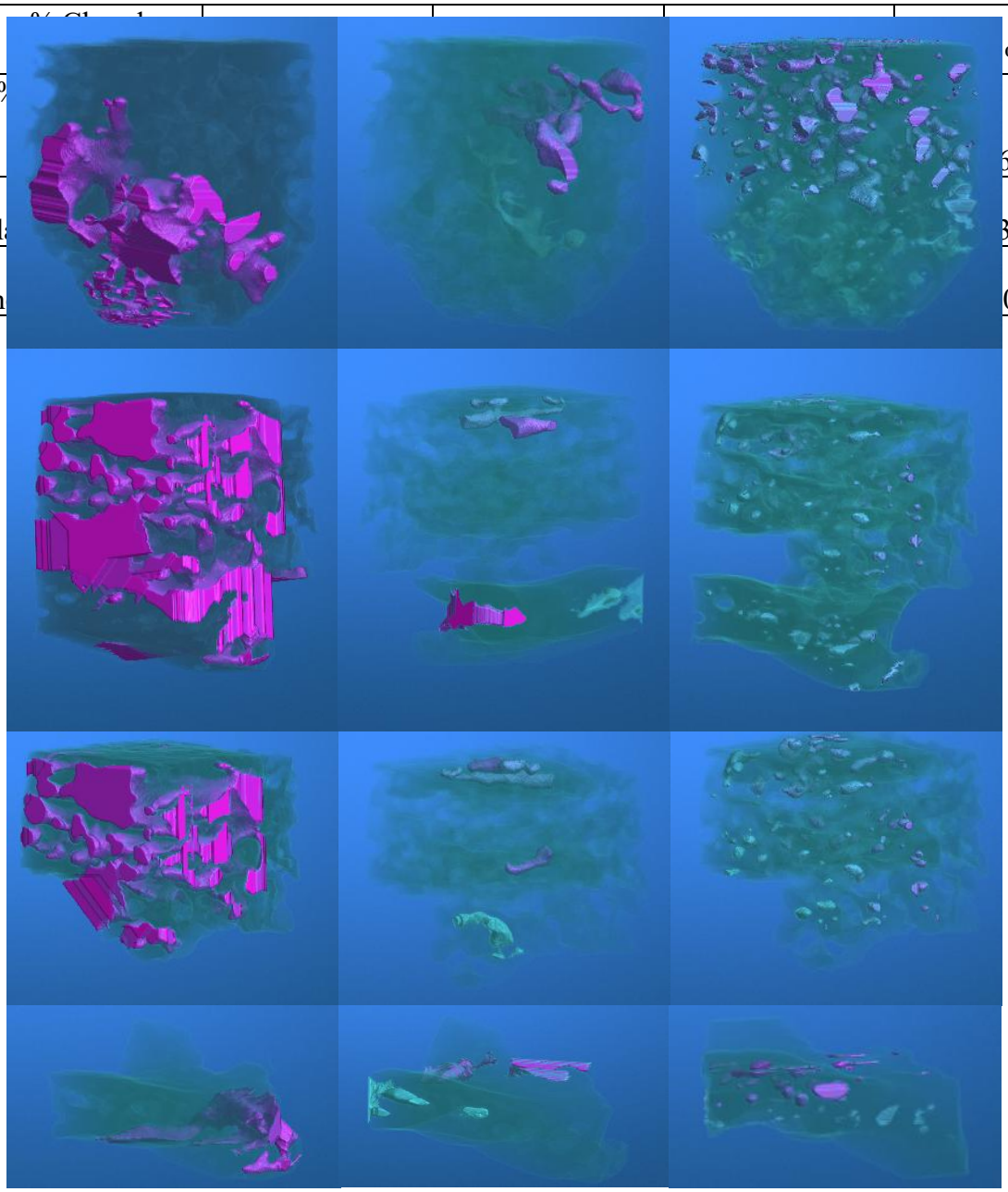

*Figure 6: 3D representation of pore networks in both cubes showing: Largest single pore network, next four largest pore networks, and remaining pore networks. The top row shows the fuel cube and the second row shows the fluff cube. The third and fourth rows show the top and bottom regions of the fuel cube separately.*

# 4 Discussion

## 4.1 Pore Size Distributions

Figure 8 summarizes pore size and overall porosity distributions for each cube. To cover the wide range of pore sizes individual pore structures were sorted into 5 categories: very small, small, medium, large, and very large. Each size category covers 1 order of magnitude in pore size. The current understanding of pore growth progression is that fission gas initially nucleates in small, isolated pores. These pores grow and merge with each other to form large, interconnected structures. At the same time, new, small, isolated pores are constantly being created. Because of this, the pore distribution from fission gas swelling is expected to consist of a small number of very large, interconnected pores, and a large number of much smaller isolated pores [1] [36]. Past metallic fuel 2D and 3D characterization show that the overall fuel porosity is expected to be mostly concentrated in large pores, but a significant amount is still contained in the small isolated pores [31] [20]. The pore distribution of the fuel cube follows this trend as can be seen in Figure 8a. Less than 0.6% of pore structures fall into the large and very large categories but they comprise over 65% of the fuel

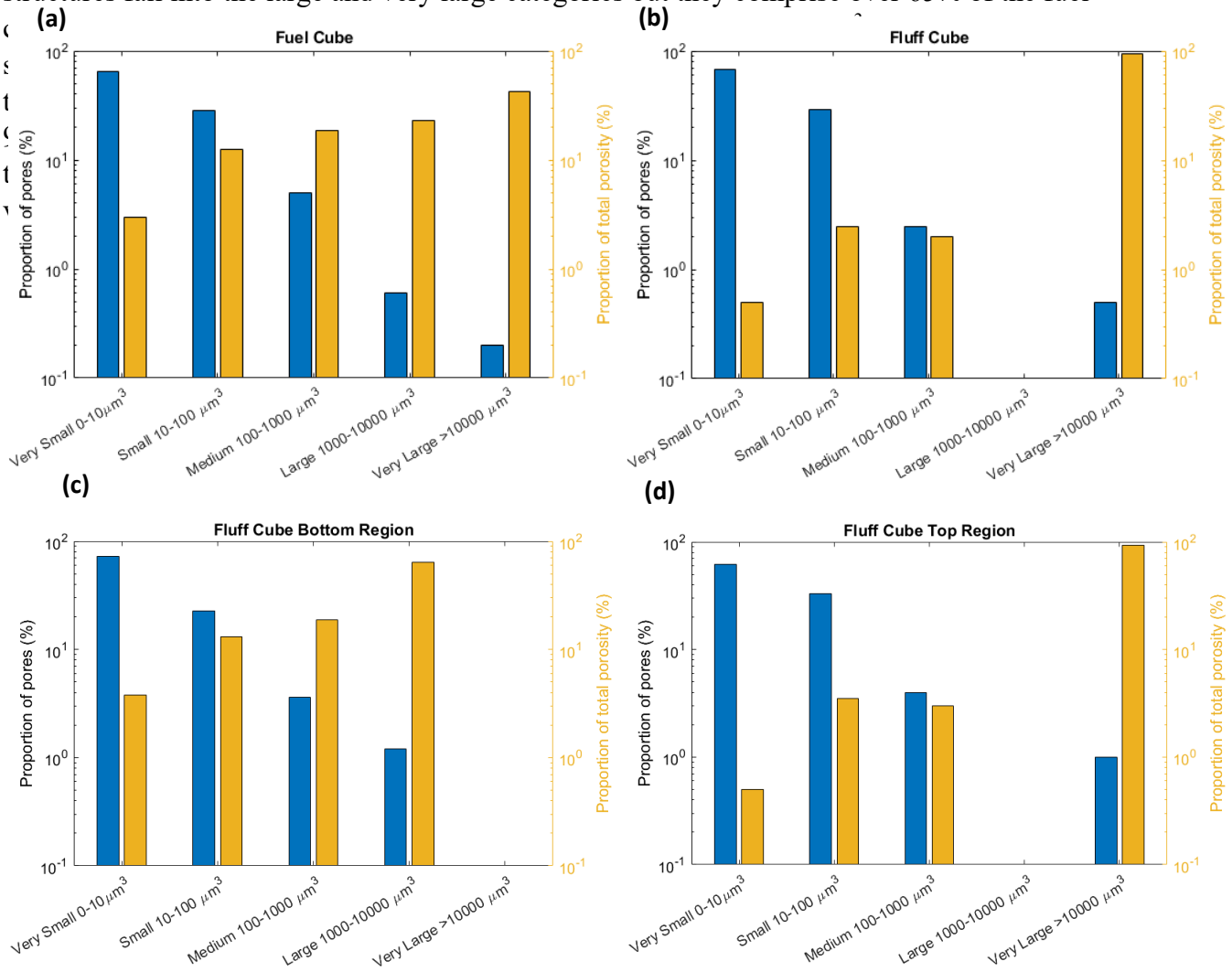


Figure 8: Pore size distributions for (a) the fuel cube, (b) the fluff cube treated as 1 unit, (c) the fluff cube top region, and (d) the fluff cube bottom region.

*Figure 7: Pore size distributions for (a) the fuel cube, (b) the fluff cube treated as 1 unit, (c) the fluff cube top region, and (d) the fluff cube bottom region.*

When the top and bottom regions of the fluff were characterized separately, they showed significant differences in pore distribution. The top region reflects the overall behavior of the fluff cube with a high total porosity dominated by a single central pore network. The bottom region more closely resembled the distribution of the fuel cube where most porosity is contained in a small number of large pore structures, but small and medium pores still contribute a significant amount. We initially thought these differences in porosity could be from differences in the concentration of fissile atoms between the top and bottom regions. If the bottom region had a lower concentration of U and Pu, then it would have produces less fission gas which would explain its lower porosity. The EDS characterizations however show minimal differences in the regions' elemental composition. Because of this, the difference in porosity between the top and bottom regions is most likely from statistical variations in local porosity since both regions are small compared to the total area occupied by fluff, particularly the bottom region.

## 4.2 Sphericity

The material phases that exist in metallic fuels during irradiation are known to have an impact on pore shape [35]. Because of this Measuring pore sphericity can give insights into the local phase structure of the fuel. α-U, which is stable at lower temperature, swells by a grain boundary tearing mechanism and forms irregularly shaped pores even at small sizes [35] [1]. Higher temperature $\gamma$ phase however forms more spherical shaped pores [10]. During irradiation metallic fuels undergo constituent redistribution where thermal gradients cause Zr to migrate to the fuel center and outer periphery. This creates a Zr depleted intermediate zone that is primarily made up of α-U [30]. PIE of irradiated metallic fuel cross sections has shown that this high α-U zone forms irregularly shaped "tear like" pore structures that are distinctly different from the pore structures that form in the more Zr rich regions [35] [31]. Pore sphericity is also known to have a negative correlation with pore size. This is because as the pores grow, they merge with surrounding pores and become more irregularly shaped. The final large, interconnected pores tend to be very irregularly shaped and exhibit low sphericity [35].

Figure 9 shows the sphericity vs volume relationship for all cubes. Every sphericity plot showed a negative relationship between sphericity and pore volume as expected. Both the fluff and fuel cubes also showed a significant quantity of small pores with low sphericities. These small, low sphericity pores could imply that there was a significant amount of α-U present in the regions the 2 cubes were taken from while DP-55 was being irradiated. This result is expected since the fuel cube was taken from the top outer periphery of DP-55 which is expected to be in the temperature range α-U is stable at during steady state operation. The region the fluff cube

was taken from was logged with liquid sodium and expected to be at a lower temperature due to the high thermal transfer from sodium and be in the temperature range α-U is stable. The presence of α-U surrounding the irregularly shaped pores in the two cubes, however; cannot be confirmed since Micro-CT scans could not acquire data on 3D elemental or crystal structure. Overall, there were minimal differences in the sphericity distribution between the fluff and fuel cubes which implies that the pore nucleation mechanisms and phase content of the two cubes are similar. The only significant difference was the large central pore that formed within the fluff cube. The top and bottom of the fluff cube also showed very similar sphericity distributions

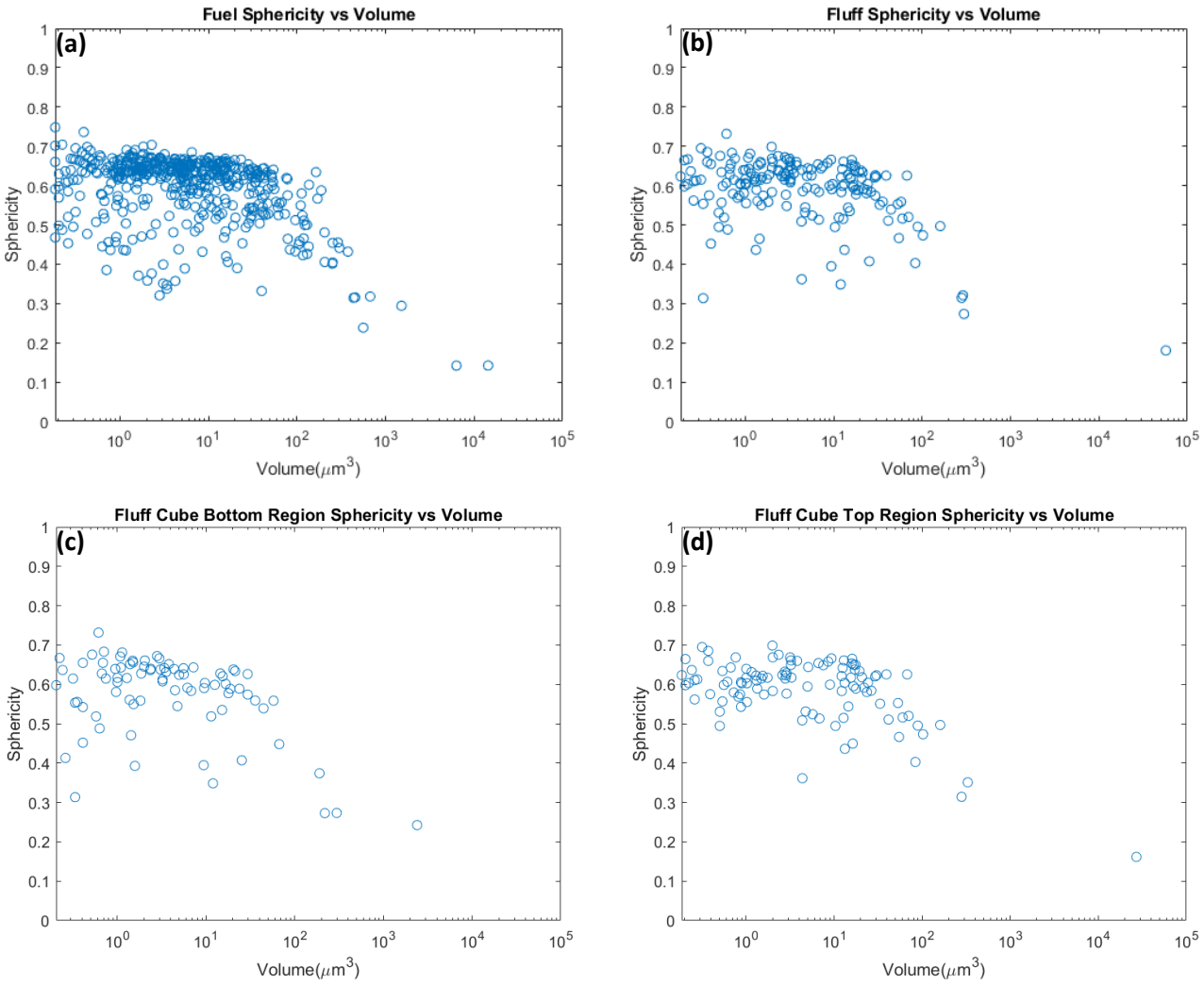


*Figure 8: Pore size vs sphericity distributions for (a) the fuel cube, (b) the fluff cube, (c) the fluff cube bottom region, and (d) the fluff cube top region.*

One of the goals of performing 3D characterization on a small cube of fluff and fuel was to determine if the differences in porosity and morphology between fluff and fuel visible in macro scale PIE also exist on the microscale. The overall higher relative porosity of fluff has been well known since early metallic fuel pin irradiations [1], but it was unclear whether the high porosity of fluff is entirely contributed to the very large interconnected pores seen in Figure 1 or if the small fuel fragments that reside in the fluff region have internal porosities that differ from

those in the bulk fuel on the micro-scale. The differing pore distributions and microscopic porosity between the two cubes indicate that the high porosity of fluff is not just caused by an increase in the space between fuel fragments, but that the fuel fragments of fluff also exhibit higher porosity. This result could show support for the creep driven formation mechanism of fluff discussed in the introduction. An increased creep rate at the top of the fuel would provide an additional driver to the formation of porosity that would impact both macro scale and microscale pore growth. Both cubes, however, were small compared to the overall fluff and fuel regions and may not fully reflect the micro-scale porosity of the fuel fragments that comprise fluff.

## Conclusion

In this work 60×60×60μm cubes were taken from the fluff and bulk fuel regions of a high burnup U-19Pu-10Zr fuel sample and characterized by micro-computed X-ray tomography and surface EDS. The EDS characterizations found minimal differences between the elemental compositions of the fluff and fuel fragments. Both were mostly made up of fuel elements in similar concentrations to as cast fuel with small, localized regions of lanthanide precipitates. Micro-CT characterizations indicated that the clear porosity differences between fuel and fluff that are clearly visible on the macro scale also exist on the micro scale. The fluff cube showed a much higher total porosity, 36%, compared to the fuel cube, 15.0%. The fluff cube also showed a significantly different pore volume distribution with almost all its porosity concentrated in a few large open pore structures, while the fuel cube showed a significant amount of porosity contained in smaller closed pores and nearly resembles previous characterizations done on bulk U-10Zr. This finding gives some support for the creep driven formation mechanism of fluff. Sphericity characterizations showed minimal differences in the pore morphologies of the fluff and fuel cube.

## Acknowledgements

This work was supported by the U.S. Department of Energy, Office of Nuclear Energy under DOE Idaho Operations Office Contract DE-AC07- 05ID14517 as part of a Nuclear Science User Facilities experiment. Accordingly, the U.S. Government retains the rights to this work and the publisher, by accepting the article for publication, acknowledges that the U.S. Government retains a nonexclusive, paid-up, irrevocable, worldwide license to publish or reproduce the published form of this manuscript or allow others to do so, for U.S. Government purposes.

## References

[1] L. C. W. T. H. B. G. L. Hofman, "Metallic Fast Reactor Fuels," Argonne National Laboratory, 1996.

[2] A. Aitkaliyeva, "Recent Trends in Metallic Fast Reactor Fuels Research," *Journal of Nuclear Materials,* 2022.

[3] D. L. P. S. L. H. J. R. K. Robert D. Mariani, "Metallic Fuels: the EBR-II legacy and Recent Advances," *Procedia Chemistry,* 2012.

[4] G. L. H. B. R. S. a. L. C. W. D. L. Porter, "Factors Controlling Metal Fuel Lifetime," in *International Conference on Rliable Fuels for Liquid Metal Reactors*, 1986.

[5] L. Walters, "Thirty years of fuels and materials information from EBR-II," *Journal of Nuclear Materials,* 1999.

[6] K. E. W. L. C. A. X. Z. A. J. W. C. B. J. D. M. W. Fidelma G. Di Lemma, "Investigation of Fuel Microstructure at the Top of a Metallic Fuel Pin after a Reactor Overpower Transient," *Journal of Nuclear Materials,* 2021.

[7] F. D. L. A. G. K. P. P. M. L. C. D. P. J. L. J Fay, "An analysis of fluff formation in metallic fuel via data analysis from EBR-II experiments and BISON fuel code modeling," *Journal of Nuclear Materials,* 2022.

[8] F. G. D. L. J. F. D. L. P. K. M. P. L. C. Andrei V. Gribok, "Qualification and Quantification of Porosity at the Top of the Fuel Pins in Metallic Fuels Using Image Processing," *Energies,* 2024.

[9] H. G. P. a. C. A. B. C. N. Jackson Jr., "Neutron Radiography of Fuel Pins," American Society for Testing and Materials, 1976.

[10] R. P. C. L. D. P. G.L. Hofman, "Swelling Behavior of U-Pu-Zr fuel," *Metallurgical Transactions A,* 1990.

[11] S. N. B. S. R. S. R. W. G. P. D. P. J.D. Hales, "Verification of the BISON Fuel Performance Code," *Annals of Nuclear Energy,* 2014.

[12] C. U. J. G. D. D. K. J. S. H. Christopher Matthews, "Fuel-cladding chemical interaction in UPuZr Metallic Fuels," *Nuclear Technology,* 2017.

[13] J. B. h. M. W. J Baumeister, "Aluminium foams for transport industry," *Materials and Design,* 1997.

[14] C. S. G. H. Casey Mckinney, "A Practical Guide to Characterizing Irradiated Nuclear Fuels Using FIB Tomography," *Micron,* 2022.

[15] C. B. S. C. V. C. D. G. C. K. H. E. M. M. M. A. D. P. a. S. R. S. Philip J. Withers, "X-Ray computed tomography," *Nature Reviews Methods Primers,* 2021.

[16] W. D. C. Richard A. Ketcham, "Acquisition, optimization and interpretation fo X-ray computed tomographic imagery: application to the geosciences," *Computers and Geosciences,* 2001.

[17] NIST, "X-Ray Mass Attenuation Coefficients," NIST, 2009. [Online]. Available: https://www.nist.gov/pml/x-ray-mass-attenuation-coefficients. [Accessed 3 December 2024].

[18] D. Swinehart, "The Beer-Lambert Law," *Journal of Chemical Education,* 1962.

[19] J. T. J. H. P. K. B. M. J. A. M. O. A. Figueroa Bengoa, "Synchrotron micro-computed tomography analaysis of neutron irradiated U-Mo fuel," *Journal of Nuclear Materials,* 2024.

[20] A. F. B. S. N. R. R. P. K. J. A. J. H. J. H. M. O. J. Thomas, "The application of synchrotron micro-computed tomography to characterize the three dimensional microstructure in irradiated nuclear fuel," *Journal of Nuclear Materials,* 2020.

[21] L. C. D. P. Daniel M. Wachs, "Behavior of Metallic Fast Reactor Fuels During an Overpower Transient," *Journal of Nuclear Materials,* 2021.

[22] R. R. K. S. M. William Chuirazzi, "Laboratory-Based Micro-X-ray Computed Tomography of energy materials at idaho national laboratory," *Journal of the Minerals, Metals and Materials Society,* 2024.

[23] R. D. H. Richard A. Ketcham, "Beam Hardening Correction for X-Ray Computed Tomography of Heterogeneous Natural Materials," *Computers and Geosciences,* 2014.

[24] L. C. D. J. W. K. L. A. Feldkamp, "Practical Cone-Beam Algorithm," *Journal of Optical Society of America A,* 1984.

[25] I. A.-C. E. F. V. K. M. L. T. P. S. P. C. R. S. S. B. S. J.-Y. T. P. T. A. C. Johannes Schindelin, "Fiji: an open source platform for biological image analysis," *Nature Methods,* 2012.

[26] T. M. Inc, *Matlab Version: 2023b,* The MathWorks Inc, 2023.

[27] S. T. E.A. Robinson, "Principles of Digital Wiener Filtering," *Geophysical Prospecting,* 1967.

[28] G. R. Bradley, "Adapting thresholding using the integral image," *Journal of Graphics Tools,* 2007.

[29] M. K. I. A.-C. F. P. C. R. P. D. J. S. J. B. S. J. R. H. S. J. S. Michael Doube, "BoneJ: Free and extensible bone image analysis in ImageJ," *Bone,* 2010.

[30] B. D. M. L. C. A. A. Thaddeus Rahn, "TEM-Based phase characterization of U-19Pu-10Zr," *Materials Research Society,* 2022.

[31] X. L. D. J. M. K. M. P. F. X. T. P. M. T. B. L. C. T. Y. Daniele Salvato, "Transmission electron microscopy study of a high burnup U-10Zr Metallic Fuel," *Journal of Nuclear Materials,* 2022.

[32] F. G. D. L. J. M. H. Luca Capriotti, "Testing fast reactor fuels in a thermal reactor: Comparison of transmutation metallic fuel alloys by scanning electron microscopy".

[33] J. M. H. Y. X. T. Y. K. R. T. K. E. W. J. A. K. A. I. H. Q. C. Michael T. Benson, "Out-of-pile and postirradiated examination of lanthanide and lanthanide-palladium interations for metallic fuel," *Journal of nuclear Materials,* 2021.

[34] M. B. J. J. David Grabaskas, "Regulatory Technology Development Plan Sodium Fast Reactor ANL-ART-38," Argonne National Laboratory, 2016.

[35] A. Y. M. S. T. B. A. W. Di Yun, "Simulation of the impact of 3-D porosity distribution in metallic U-10Zr fuels," *Journal of Nuclear Materials,* 2014.

[36] H. L. W. Z. J. W. Jingyu Guo, "Fission Gas Behaviors and Relevent Phenomena in Different nuclear fuels: a review of models and experiments," *Frontiers in Energy Research,* 2022.

## APPENDIX A: FIB Damage to Fluff and Necessary Correction to Micro-CT Data Analysis

When the fluff cube was being mounted, beam drift caused the Xe ion beam to mill into its top surface as shown in Figure 10. The damaged region starts 42 $\mu$m from the front face, is 6 µm wide, and about 40 µm long. After noticing the damage, we decided to not mill off the damaged region by ion beam and instead move forward with the planned Micro-CT characterization. During Micro-CT data analysis, the damaged region was identified in the fluff reconstruction and excluded from any of the pore structure characterizations. Figure 11 shows the 3D reconstruction of the fluff cube with the damaged region cropped out.

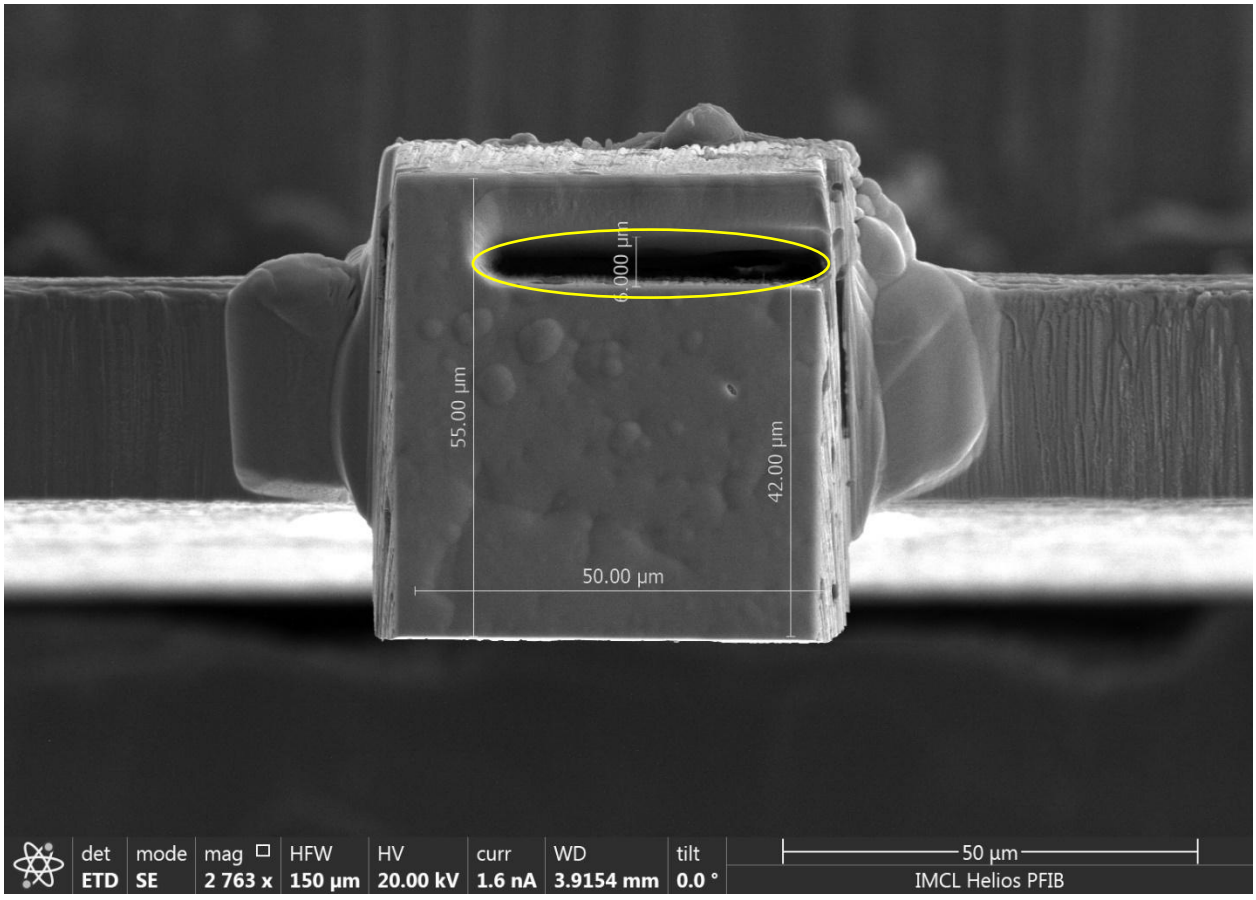

*Figure 9: Fluff Cube Top Surface with FIB Damage Identified*

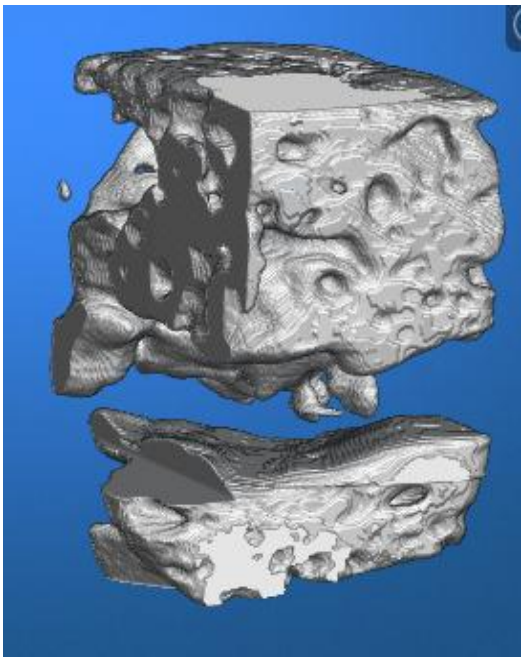

*Figure 10: 3D Reconstruction of the Fluff Cube with the Damaged Region Cropped Out*

## Appendix B: Image Stack Segmentation Evaluation

The pore and solid fuel segmentations reported in this paper were calculated using the adaptthresh algorithm in the MATLAB image analysis toolbox [26] [28]. The quality of these segmentations was evaluated by manually segmenting a subset of 3 images from both the fluff and fuel cube .tiff stacks by hand and comparing the adaptthresh segmentation to the manual segmentations with eq 3. The results of this are summarized in Figure 12, Figure 13, and Table 4. The resulting accuracies were all greater than 94%.

*Equation 3*

$$Accuracy = \frac{Pixels\ Correctly\ Identified}{Total\ Number\ of\ Pixels\ in\ the\ Image}$$

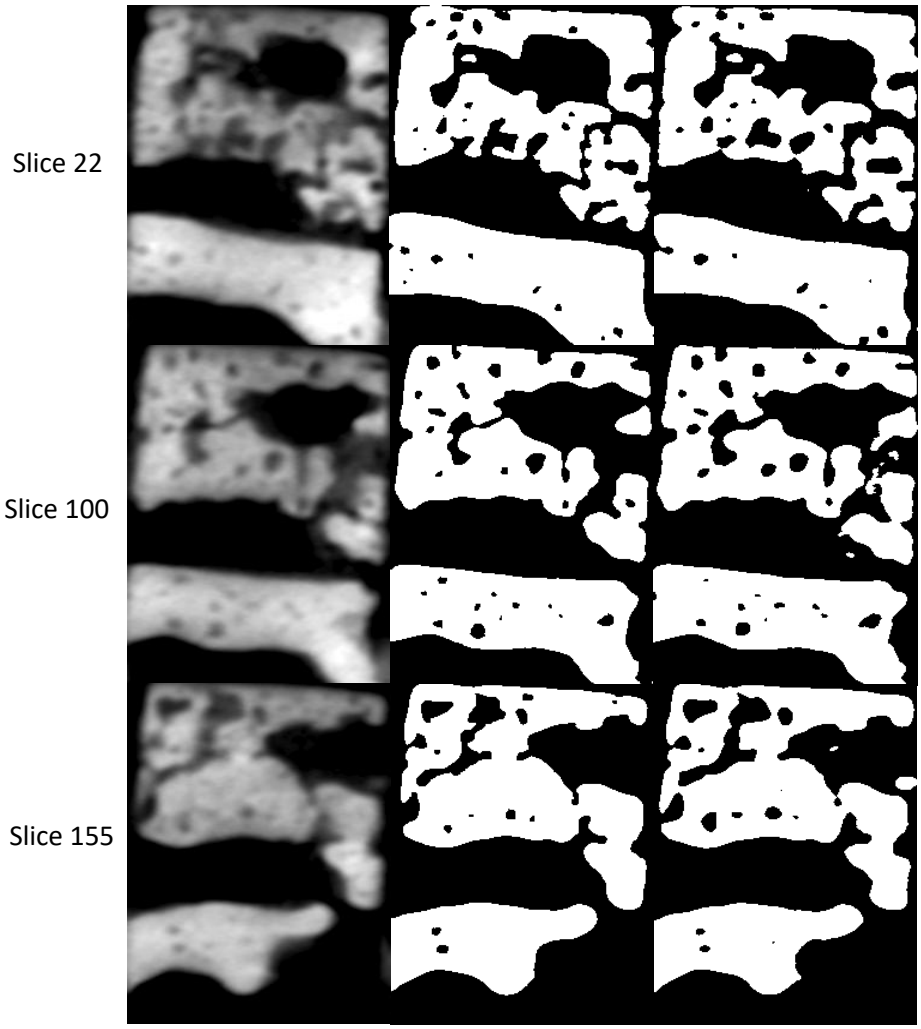


*Figure 11: Fluff cube segmentation evaluation. The first column shows the reconstruction produced by the Xradia after image smoothing, the middle column shows the manual segmentation, and the last column shows the adapthresh segmentation.*

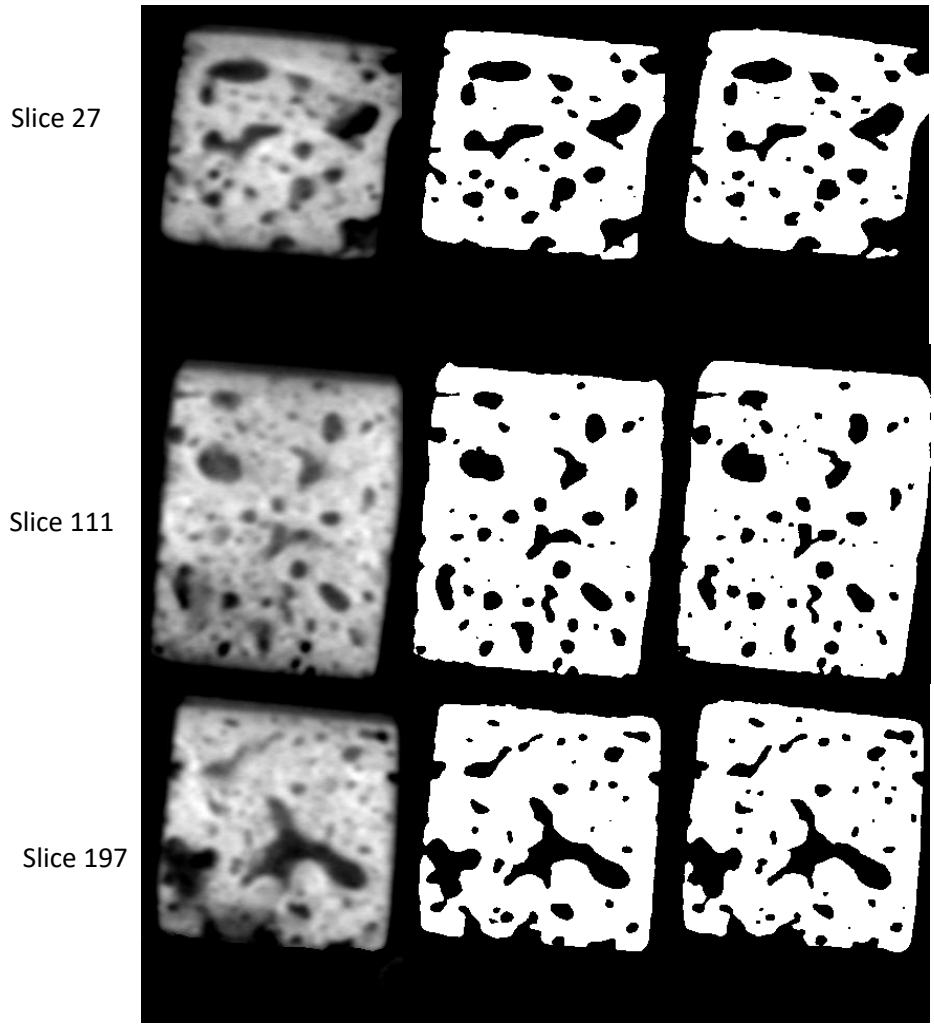


*Figure 12: Fuel cube segmentation evaluation. The first column shows the reconstruction produced by the Xradia after smoothing, the middle column shows the manual segmentation, and the last column shows the adapthresh segmentation.*

*Table 4: Segmentation Evaluation Results*

| Fluff | | Fuel | |
|---|---|---|---|
| Slice | Accuracy | Slice | Accuracy |
| 69 | 95% | 27 | 97% |
| 100 | 95% | 111 | 94% |
| 155 | 96% | 197 | 96% |